Journal of Colloid and Interface Science 468 (2016) 1–9

Contents lists available at ScienceDirect

Journal of Colloid and Interface Science

journal homepage: www.elsevier.com/locate/jcis

Template method to controllable synthesis 3D porous $NiCo_2O_4$ with enhanced capacitance and stability for supercapacitors

Yang Bai, Ranran Wang, Xiaoyu Lu, Jing Sun *, Lian Gao

The State Key Lab of High Performance Ceramics and Superfine Microstructure, Shanghai Institute of Ceramics, Chinese Academy of Science, 1295, Dingxi Road, Shanghai 200050, PR China

GRAPHICAL ABSTRACT

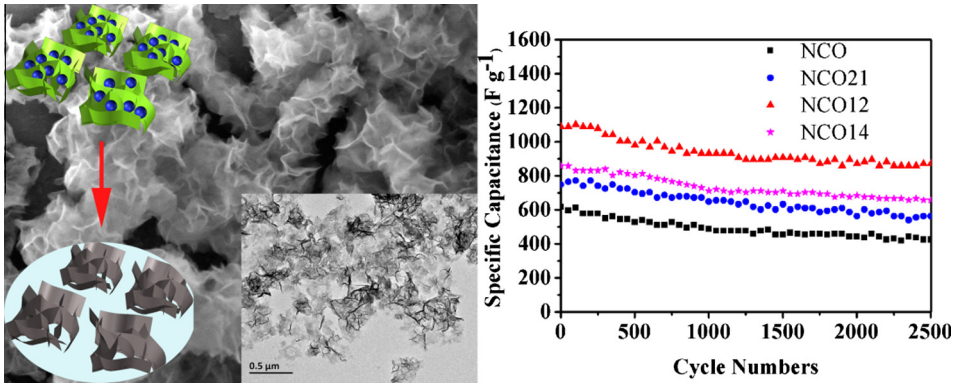

ARTICLE INFO

Article history:
Received 8 September 2015
Revised 17 December 2015
Accepted 11 January 2016
Available online 12 January 2016

Keywords:
3D porous structure
Template method
SiO_2
Nickel cobaltite
Supercapacitors
Energy storage

ABSTRACT

We present a facile template method to fabricate $NiCo_2O_4$ (NCO) composites with 3D porous structure as electrodes for supercapacitors. SiO_2 sol is used as the template to prevent the aggregation of NCO and construct the porous structure with high specific surface area. Meanwhile, the binary metal oxides not only inherit the merits of single nickel oxides or cobalt oxides, but also show superior properties to promote the capacitance. The uniform structure of NCO12 (SiO_2/NCO = 1:2) is obtained through controlling the mass ratio of SiO_2 and NCO. Owing to the dual advantages of porous structure and binary system, NCO12 composites exhibit highly enhanced electrochemical performance compared with those of directly prepared NCO, NCO21 (SiO_2/NCO = 1:0.5) and NCO14 (SiO_2/NCO = 1:4). The specific capacitance of NCO12 composite is about 1389 F g^{-1} at 1 A g^{-1}. At 4 A g^{-1}, the capacitance is still as high as 1090 F g^{-1} together with capacitance retention of 80% over 2500 cycles. The capacitance and stability are higher than those of most previously reported pure NCO composites, which make it a very promising electrode material for energy storage.

1. Introduction

As alternative energy storage devices, electrochemical capacitors (ECs) have drawn increasingly attentions owing to their higher power density and longer cycle life than batteries, and higher energy density than conventional capacitors [1]. They are commonly appropriate for applications which require short-term power or act as peak power assistance for batteries [2,3]. To better satisfy the practical application, high performance ECs are needed, which are determined by the high capacitance and cycling stability of electrode materials [4]. Transition metal oxides (TMOs) are suitable

* Corresponding author.
E-mail address: jingsun@mail.sic.ac.cn (J. Sun).

http://dx.doi.org/10.1016/j.jcis.2016.01.020
0021-9797/

candidates for ECs electrode materials due to their high theoretical capacitance, such as NiO (2573 F g^{-1}) [5], Co_3O_4 (3560 F g^{-1}) [6], and MnO_2 (1380 F g^{-1}) [7]. Their multiple redox states and easily synthetic process have attracted more and more interest from both academic and industrial consideration. However, the real capacitance is still far from their theoretical values and the stability (capacitance retention after long cycle tests) is poor because of the less active sites and the intrinsic low conductivity of oxides. So far, a major challenge in this field is to improve the electric properties of these metal oxides.

To solve these problems, high specific surface area, controlled porosity, and high electric conductivity of TMOs are required [8]. An effective strategy is to construct the component and structure of TMOs. It is well known that the binary system can inherit the merits of both single component and the atom substitution will increase electrical conductivity [9–12]. Meanwhile, the binary oxides can exhibit superior performance, such as higher electrochemical activity, tendency to form a variety of nanostructures, and higher electroactive surface areas [13,14]. Among so many TMOs, nickel and cobalt were easy to form binary oxides with high performance due to their miscible ions in aqueous solution with nearly identical physical and chemical properties [15,16]. When the Ni/Co atom ratio was 1:2, the spinal nickel cobaltite ($NiCo_2O_4$, NCO) was formed. The conductivity of NCO was two orders higher than those of pure NiO or Co_3O_4 [9], which was beneficial to obtaining electrodes with higher rate capacity (capacitance retention at high charge–discharge current density versus low current density) and stability. Xiao et al. prepared sea urchin-like NCO composites with the specific surface area of up to 198.9 m^2 g^{-1}, exhibiting higher specific capacitances of 658 F g^{-1} compared to pure NiO and Co_3O_4 [17]. Wei et al. synthesized the NCO aerogels by sol–gel process with the maximum capacitance of 1400 F g^{-1} [18]. These excellent researches demonstrated that the NCO did have superior performance. However, their aggregated morphologies and compact structures were not good for better stability and faster electric transport.

Three-dimensional porous structure has its unique advantages for energy storage. It can provide a continuous electron pathway to ensure good electrical contact as well as facilitate ion transport by shortening diffusion pathways [19]. Besides, the porous structure can also enlarge the specific surface area to increase the active sites for high capacitance. There were many methods to fabricate the 3D porous structure materials. Liu et al. synthesized 3D porous $NiCo_2O_4$ hetero-structure array on nickel foam get a high capacitance of 1089 F g^{-1} with high stability [20]. Wang et al. prepared 3D Ni_xCo_{1-x} oxides with a large specific capacitance of 1523 F g^{-1}, and the capacitance retention was nearly 100% after 1000 cycles [21]. All the results demonstrated that the 3D structure was in favor of obtaining high capacitance and stability materials. However, the solvothermal method was not easy to control and the structure of products could hardly be adjusted. The deposition process could obtain different structures, but the matrixes were required. In this case, the growth is restricted by such matrix and the mass of load is low. What's more, the reaction yield of these methods was too low to meet the actual requirement, which brought troubles for further research. In order to obtain high performance electrode materials and develop the ECs, these issues are urgently needed to be solved and novel and efficient method should be introduced. The template method can improve the dispersion stability of the reaction solutions and control the size and shape of products more precisely. Furthermore, the reaction yield of template method is large.

In this study, we synthesized 3D porous nickel–cobalt binary oxides using silicon dioxide sol as the template via a facile method under mild condition. In the synthesis process, SiO_2 sol was chosen due to its low cost and reliable removal process. The metal ions were efficiently deposited on negative-charged SiO_2 sol by electrostatic attraction. With the help of SiO_2, the aggregation of NCO particles was successfully avoided, which increased the specific surface area and active sites. Meanwhile, porous structure was obtained, which is in favor of the electrons and ions transmission. The electrochemical performance of the 3D porous composites can be tailored by simply adjusting the relative dosage of SiO_2 in the synthesis process. The unique structure enables fast charge–discharge response and displays enhanced the maximum specific capacitance of 1389 F g^{-1} at 1 A g^{-1}. The development of this method to make 3D porous structure can be applied for other TMOs and may have a positive impact for developing high performance ECs based on pseudocapacitive materials.

2. Materials and methods

2.1. Materials

SiO_2 sol in ethylene glycol (30 wt.%) was purchased from Alfa Aesar. Nickel nitrate hexahydrate ($Ni(NO_3)_2{\cdot}6H_2O$, AR), cobalt nitrate hexahydrate ($Co(NO_3)_2{\cdot}6H_2O$, AR), urea (CON_2H_4, AR), were all purchased from Shanghai Sinopharm Chemical Reagent Co., Ltd. (Shanghai, China).

2.2. Synthesis of 3D porous NCO composite

In the typical experiment, 1 ml SiO_2 sol (contained about 370 mg SiO_2) was added into 100 ml distilled water slowly under stirring gently. The SiO_2 sol remained stable during this process and the Tyndall effect can be observed (Fig. S1). The solution with 3 mmol $Ni(NO_3)_2{\cdot}6H_2O$ and 6 mmol $Co(NO_3)_2{\cdot}6H_2O$ in 50 ml water was added to the above SiO_2 sol drop by drop. Then, 3 g urea was slowly added. After stirring for 30 min, the mixture was refluxed at 100 °C for 12 h in an oil bath. The reaction product was filtrated and washed with distilled water and ethanol successively for several times, and finally dried and heated at 300 °C for 1.5 h in air. The earthy yellow products were etched in 2 M NaOH aqueous solution at 80 °C and the etch solution was refreshed every 30 min. After several times, the 3D porous structure NCO was obtained and denoted as NCO12 for the mass ratio of SiO_2 and NCO of 1:2 in calculation. For comparison, pristine NCO powder, which was denoted as NCO, was prepared in nearly the same way as NCO12, except without SiO_2 addition. The samples with mass ratio of 1:0.5 and 1:4 for SiO_2 and NCO also were prepared, which were denoted as NCO21 and NCO14, respectively.

2.3. Characterization

The phase composition and crystalline structure were characterized by Powder X-ray diffraction (XRD, Rigaku D/Max 2200PC, Cu Kα). The morphology and structure of the products were analyzed by field-emission scanning electron microscope (FE-SEM, Magellan 400) and transmission electron microscope (TEM, JEOL JEM-2100F). The nitrogen adsorption isotherms of the powders were measured on Micromeritics Tristar 3000 porosimeters at 77 K.

The electrochemical properties of the materials were characterized by three-electrode method in 2 M KOH aqueous solution at room temperature. The working electrode was prepared as follows. Active material, carbon black and polyvinylidene fluoride (PVDF) binder in weight ratio of 80:10:10 were mixed in ethanol, and then 5 mg electrode powders were pasted onto a nickel foam current collector (1 cm × 1 cm). A platinum wire was used as the counter electrode and an Hg/HgO electrode worked as the reference electrode. The electrochemical impedance spectrum (EIS) was tested

by applying an AC voltage with 5 mV amplitude in a frequency range from 10 mHz to 100 kHz on Par 2273 Potentiostats Electrochemistry Workstation (U.S.A). The cyclic voltammetry (CV) at 0–0.65 V were measured on CHI660D Workstation (Shanghai, China). The galvanostatic charge and discharge tests were carried out in the potential range of 0–0.55 V on a LAND CT2001 battery tester. The specific capacitances Cs were calculated from the galvanostatic discharge curves using the equation [22,23]: $C_s = I \cdot t / m \cdot \Delta V$, where I, t, ΔV, and m are the constant current (A), discharge time (s), total potential deviation (V), and mass of active materials (g), respectively.

3. Results and discussion

The synthesize process of the 3D porous NCO composites is shown in the Fig. 1. The SiO_2 nanoparticles are negatively charged in the Colossal (Table S1). When the metal cations (Ni^{2+} and Co^{2+}) are added into the system, they will be adsorbed by the SiO_2 nanoparticles due to electrostatic attraction effect and chemical forces of surface complexation. The size of metal ions is much smaller than that of the SiO_2 particles, so they will attach on the surface of SiO_2. The electronegativity of the composites decreases but still keeps negative, demonstrating that the thickness of metal ions on SiO_2 particles is estimated to be several atomic layers. For one hand, the high stability of sol can be kept well. For another, the nucleation of metal ions will happen on the surface of SiO_2 and hydroxides grow along the surface of SiO_2 to form thin slices. At the heating stage, OH^- ions are continuous supplied by the hydrolysis of urea. Thus, the metal ions combine with OH^- to form hydroxide. The SiO_2 nanoparticles are surrounded by Ni–Co binary hydroxides (NCH) to form a core–shell structure, which will avoid the aggregation of the NCH during the growth process. During the following thermal treatment step, the NCH transforms into nickel cobaltite (NCO) through the dehydration process. After the etching process, the SiO_2 nanoparticles are removed via the reaction with NaOH and the pores are formed. Due to the high stability of NCO in the NaOH solution, the porous structure can be kept well.

The XRD patterns are measured to confirm the crystal structure of products. As shown in Fig. 2, the NCO composite shows clear characteristic peaks at 18.9°, 31.1°, 36.7°, 44.6°, 59.1°, and 64.9°, which agree well with standard diffraction card of face-centered-cubic $NiCo_2O_4$ (JCPDS card No. 73-1702). The peaks of NCO21, NCO12, and NCO14 samples also can match with the NCO sample, which means that these samples are also $NiCo_2O_4$. However, these samples show weak characteristic peaks. Fig. S2 demonstrates that the EG and NaOH have no effect on changing the crystallinity of NCO. Thus, this phenomenon is probably caused by the addition of amorphous SiO_2 and nano-size effect of thin sheets.

To characterize the morphology and superior structure of products, TEM images are taken (Fig. 3). From these images, the effects of SiO_2 template and the synthesis process can be understood clearly. Fig. 3a displays the morphology of NCO without the addition of SiO_2. An aggregated structure is observed clearly. The aggregate is made up of small NCO nanoparticles with the size of about 5 nm. This compact structure is bad for increasing the active sites for redox reaction. Fig. S3 shows the single effect of ethylene glycol to the morphology. NCO1, prepared with the addition of 1 ml ethylene glycol (EG) to replace the SiO_2 sol in the synthesis process, grows into nanorods and aggregates together to form a similar block structure. However, when the SiO_2 sol is added into the system, the morphology and structure of NCO12 is changed significantly (Fig. 3b). NCO12 transforms from particles to thin nanosheets which are coated on the SiO_2 nanoparticles. The size of SiO_2 particles are 40–80 nm (Fig. S4). After the removal of SiO_2, pores with size of 40–80 nm will be formed (Fig. 3c). With the help of SiO_2, NCO12 is not aggregated anymore and a 3D porous structure is obtained which increases the specific surface area and active sites. Fig. 3d exhibits the select area electron diffraction (SAED) of NCO12. Only two dim diffraction rings can be observed, which are associated to the (220) and (422) planes, respectively. The diffraction rings demonstrate that the composite crystallizes into cubic structure with a weak crystallinity, which is associated with the XRD results.

The microstructure will further affect the electrochemical performance. And the relative dosage of SiO_2 template can affect the morphology and microstructure of the final products. Thus, samples with different SiO_2/NCO ratios are prepared. Fig. 4 shows the SEM images of NCO (a and b), NCO21 (c and d), NCO12 (e and f), and NCO14 (g and h) composites, respectively. For NCO samples (Fig. 4a), a compact structure can be observed clearly, the NCO particles aggregates to form a bulk structure. Even in the high magnification images (Fig. 4b), no pores can be found. When the SiO_2 is used as template, the morphology is changed a lot. All the samples show nanoflower structures, which are made up of nanosheets. As

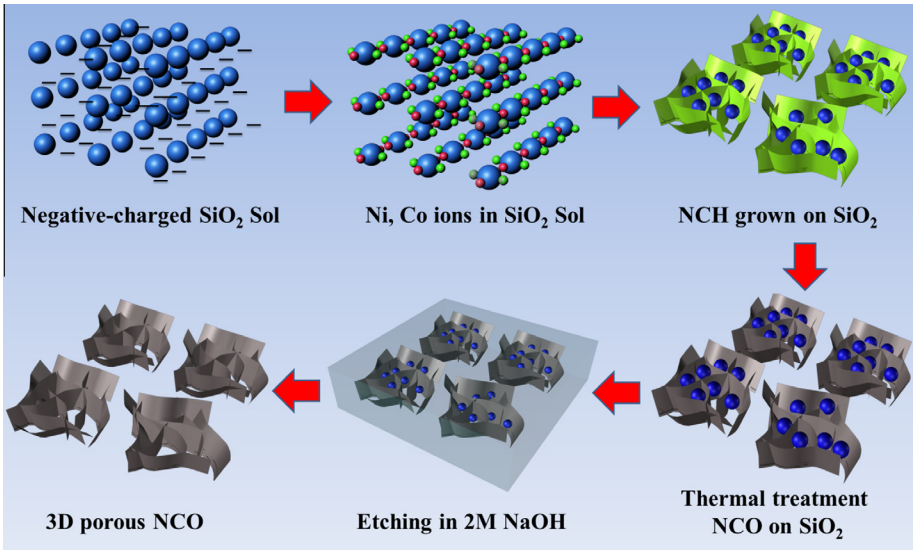

Fig. 1. The schematic illustration for the formation of 3D porous NCO composites.

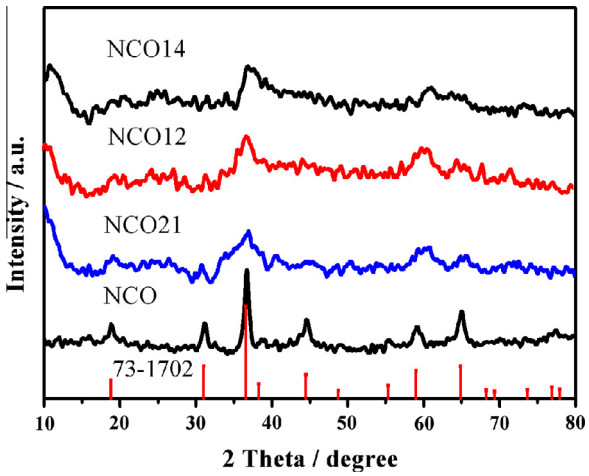

Fig. 2. The XRD patterns of NCO, NCO21, NCO12, and NCO14 composites.

seen from Fig. 4c, the aggregation of NCO21 is heavily weakened, but the structure is not uniform. The NCO21 nanosheets are large and curly and the network does not appear (Fig. 4d). As the dosage of NCO increasing, a continuous 3D porous structure is obtained (Fig. 4e). The NCO12 nanosheets are smaller than those of NCO21 samples (Fig. 4f). The pores in the NCO12 samples are about 40–80 nm. Although the nanosheets of NCO14 are similar with those of NCO12, they display a compact structure and the nanoflowers are much bigger (Fig. 4g and h). It is worth noting that the dosage of SiO_2 has affected the porous structure. When the dosage of SiO_2 is excessive, metal ions cannot cover all the surface of each SiO_2 particles. As a result, the NCO on each SiO_2 cannot connect together to form the network. In that case, the effect of SiO_2 is just to prevent the NCO sheets from aggregating. When the dosage of SiO_2 is inadequate, the unit of NCO nanoflowers will be connected by the free metal ions to make a tight structure.

Apart from the morphology, the specific surface area (SSA) and pore size distribution are also important for the electrochemical performance. Large SSA means more surfaces will be exposed in the electrolyte and more active sites to take part in the redox reaction. The pore size affects the electrolyte ions whether could enter into the inside of materials to react with active sites. Literatures have reported that the appropriate pore sizes for supercapacitor ranged from 2 to 5 nm [24,25]. As shown in Fig. 5, all the samples exhibit typical Langmuir type *IV* characteristics with an obvious hysteresis loop, indicating that the samples contain a certain amount of mesopores [26]. The hysteresis loop of NCO is H3 type (Fig. 5a), suggesting that certain aggregation happens among the particles. The SSA of NCO calculated by BET method is the smallest, only 124 $m^2 g^{-1}$. Fig. 5b shows the pore size distribution of NCO. The distribution is wide and micropores with size of 36 nm exist. Contrary to the NCO, the other three samples exhibit H1 type hysteresis loop (Fig. 5c, e, and g), which means that the distribution of pores is uniform and their size is relative small. For NCO21, although the structure is more dispersive, no network forms and the number of pores is too less to enlarge the SSA. Then, its SSA is just a little larger than that of NCO. For NCO12 and NCO14, the porous structures will facilitate the increasing of SSA. As a result, their values are much higher than that of NCO. Besides, the aggregation in NCO14 makes its SSA decrease. Through calculating, the SSA of NCO21, NCO12, and NCO14 are 142.5, 240.3, and 215.6 $m^2 g^{-1}$, respectively. The pore sizes of all the samples are similar at around 3.85 nm (Fig. 5d, f, and h), which just falls within the appropriate range. The high SSA can provide more active sites for redox reaction, which is responsible for high capacitance.

To further certify the superiority of 3D porous structure NCO as an electrode for ECs, electrochemical performance of NCO, NCO21, NCO12, and NCO14 are measured by using CV and galvanostatic charge–discharge test, respectively. Fig. 6a shows the CV curves

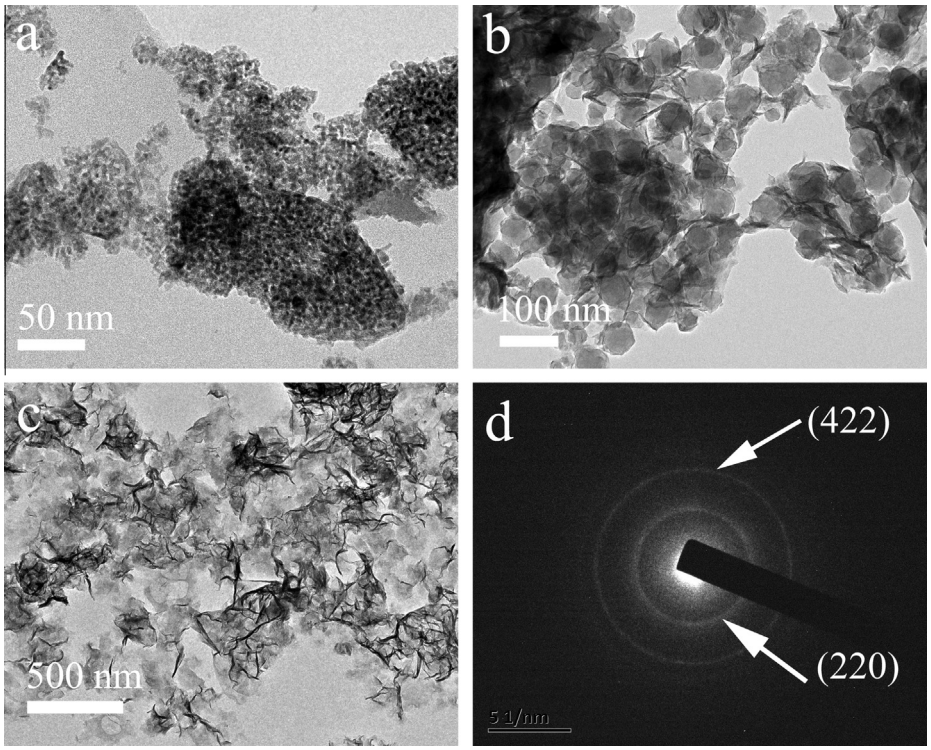

Fig. 3. TEM images of NCO without addition of SiO_2 (a), NCO12 before etching (b), final products of NCO12 (c) and the SAED of final NCO12 (d).

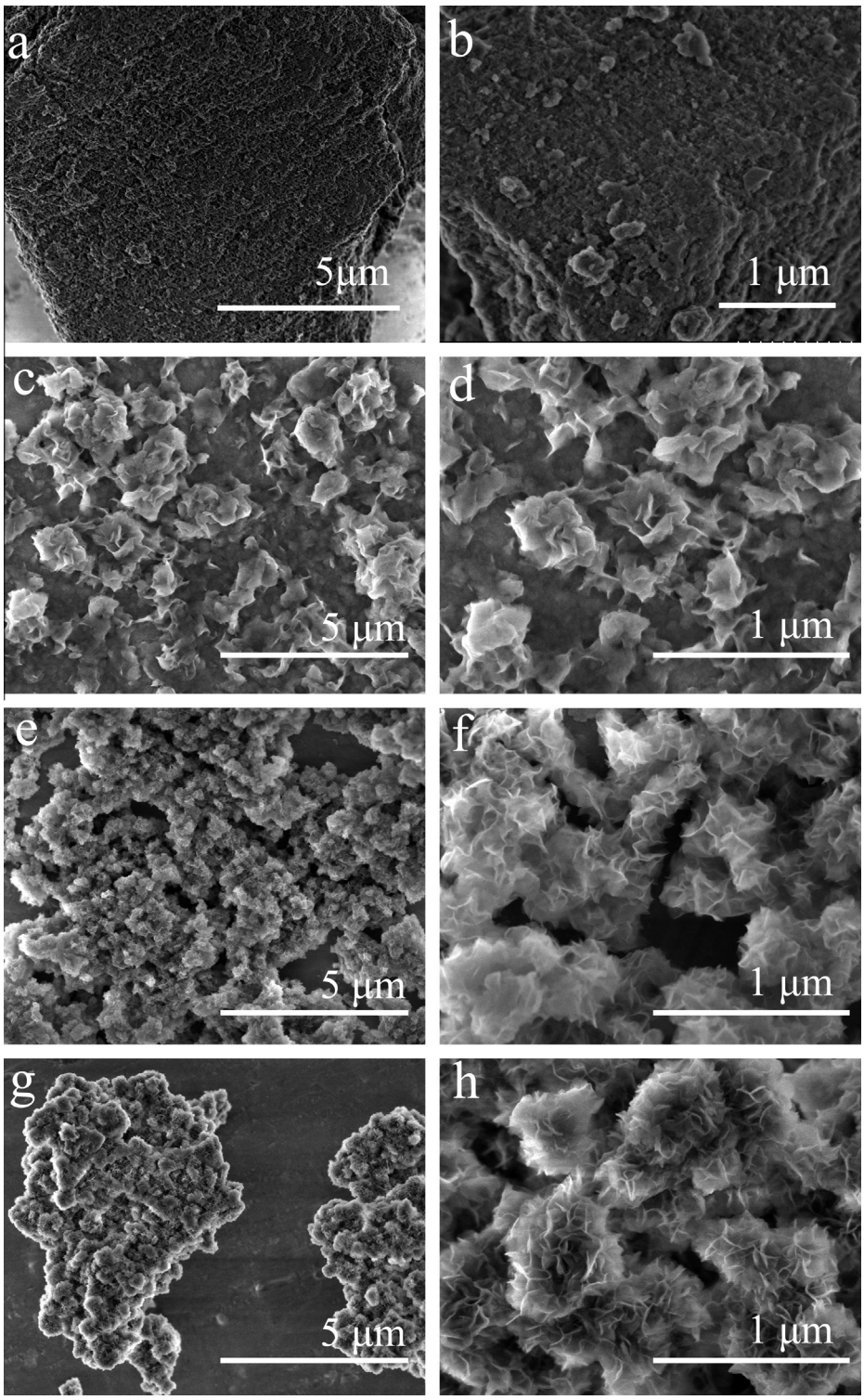

Fig. 4. SEM images of NCO (a and b), NCO21 (c and d), NCO12 (e and f), and NCO14 (g and h).

of NCO, NCO21, NCO12, and NCO14 at 5 mV s^{-1}. Two distinctive redox couples are observed on the CV curves of NCO21, NCO12, and NCO14, corresponding to the faradic reactions of M–O/M–O–OH (M represents Ni and Co ions) [1,27]. According to the equation for specific capacitance ($C = \int IdV/2\Delta vs$), a larger area surrounded by the CV curve relates to a higher specific capacitance. The CV curve of NCO exhibits the smallest area with only one redox couple, demonstrating the lowest specific capacitance. It is due to less active site caused by the tightly compact structure with the lowest SSA. Active sites taken part in the redox reaction are less, so the CV peaks of the two oxides cannot appear completely. For NCO12, its CV curve displays the largest area due to its unique porous structure with the largest SSA to provide more active sites for redox reaction. Furthermore, the porous structure owns the 3D

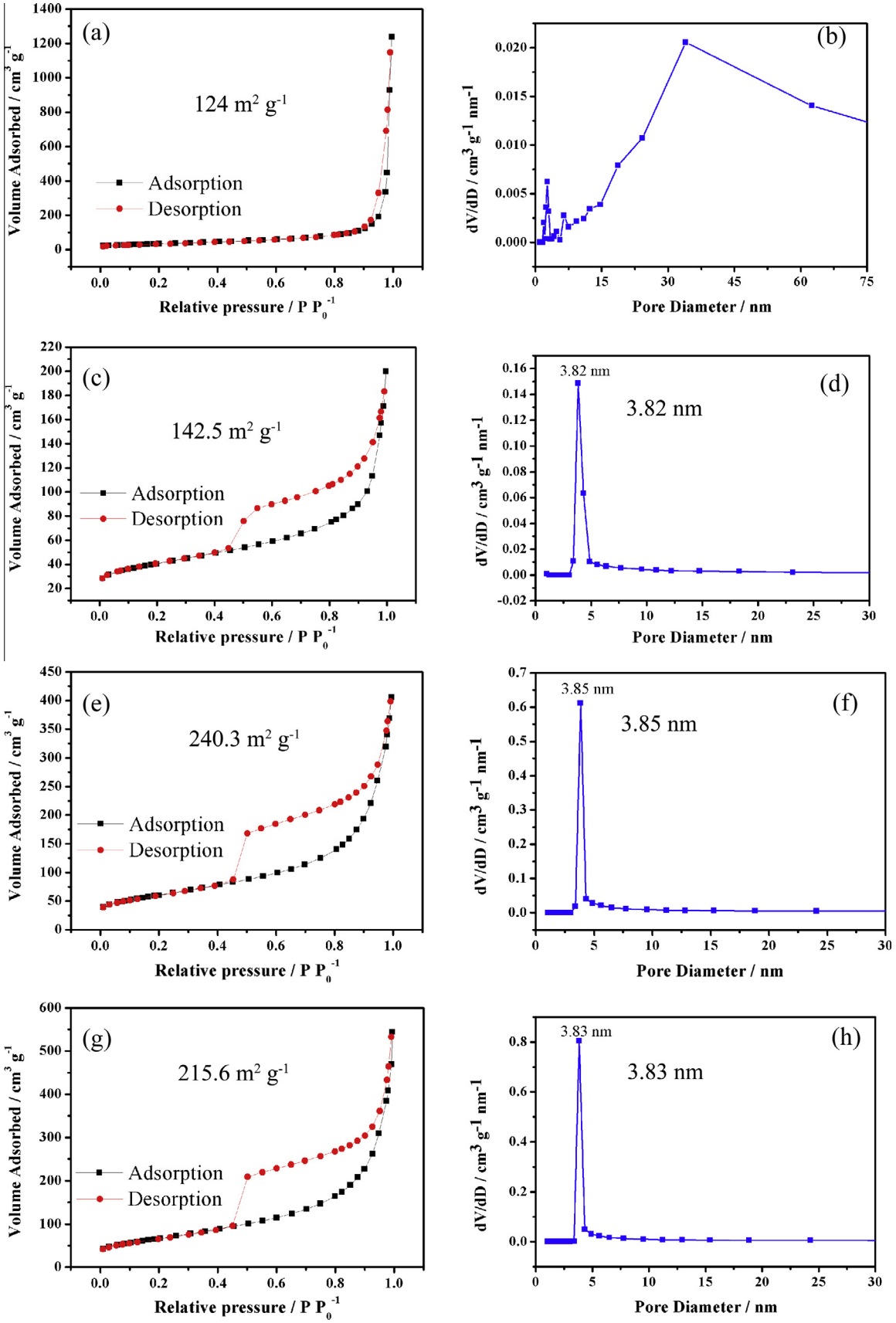

Fig. 5. N_2 adsorption–desorption isotherms and the BJH pore size distribution on the basis of the desorption branch of NCO (a and b), NCO21 (c and d), NCO12 (e and f), and NCO14 (g and h).

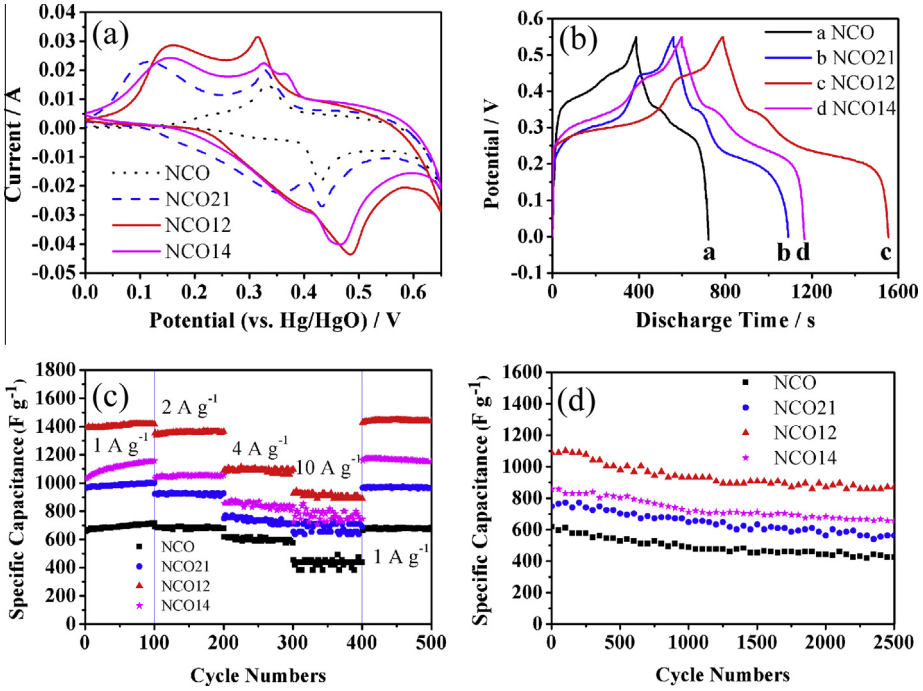

Fig. 6. (a) CV curves of NCO, NCO21, NCO12, and NCO14 electrodes at a scan rate of 5 mV s^{-1}. (b) The galvanostatic discharge curves of NCO, NCO21, NCO12, and NCO14 electrodes at 1 A g^{-1}. (c) Rate capacitance of NCO, NCO21, NCO12, and NCO14 electrodes with increasing current densities. (d) Cyclic performance of NCO, NCO21, NCO12, and NCO14 electrodes at 4 A g^{-1}.

network, which is in favor of electron transport. Thus, higher specific capacitance and electrochemical reactivity of the NCO12 sample are expected.

Fig. 6b displays the galvanostatic discharge curves of NCO, NCO21, NCO12, and NCO14 electrodes at 1 A g^{-1}. All the samples show typical pseudo-capacitive behavior with highly nonlinear discharge curves, which is consistent with the CV curves. It is worth to notice that the discharge curve of all the samples exhibited two inflexions, which are consistent with the two reactions of Ni and Co atoms. The discharge time is controlled by the rate of alkali ions diffusing into and out of the surface of the electrode [28]. Thus, the longer discharge time is, the higher the capacitance is. The longest discharge time of NCO12 illustrates the highest capacitance, which is associated with the CV results. Galvanostatic charge–discharge test at different current densities are conducted to further analyze the electrochemical performance of NCO, NCO21, NCO12, and NCO14 electrodes. Fig. 6c exhibits rate capacitance of all the electrodes with increasing current density. Under the same conditions, the specific capacitance of the NCO12 electrode is much higher than those of NCO, NCO21, and NCO14 electrodes. Through calculation, the specific capacitances at 1 A g^{-1} are 658, 965, 1389, and 1033 F g^{-1} for NCO, NCO21, NCO12, and NCO14, respectively. Generally, the capacitance decreases with the increase of the current density. The specific capacitances of NCO, NCO21, and NCO14 drop to 618, 749 and 858 F g^{-1} at 4 A g^{-1}, respectively, while the specific capacitance of NCO12 still remains 1090 F g^{-1} at the same current density. Even at high current density of 10 A g^{-1}, the specific capacitance of NCO12 is still as high as 927 F g^{-1}, which is much higher than those of other three electrodes. Fig. 6d displays the cyclability at 4 A g^{-1}. Over 2500 cycles, the capacitance of NCO12 is still as high as 871 F g^{-1}, which benefits from the uniform 3D porous structure. The capacitance retention ratios of NCO, NCO21, NCO12, and NCO14 are 69%, 75%, 80%, and 76%, respectively. The high capacitance and good stability of NCO12 are higher than those of similar systems in most reported literatures [29–31], making it a promising material for ECs.

To better understand the advantages of porous structure, the electrodes are subjected to AC impedance measurements to analyze the electron transport properties of these samples. Fig. 7 shows the Nyquist plots of NCO, NCO21, NCO12, and NCO14 electrodes. Each spectrum displays a depressed semicircle in high-frequency region and a straight line in low-frequency region. It is well accepted that the semicircle corresponds to the charge transfer resistance, which is related to the surface area and electrical conductivity [32,33]. NCO electrode exhibits largest semicircle, indicating that NCO electrode has highest charge transfer resistance. The other three electrodes display the much smaller semicircles. It is because that the compact structure disappeared and the SSA are much enhanced to make more tunnels for electron transport and more available active sites decrease the charge transfer resistance. The straight line reflects the diffusion of the

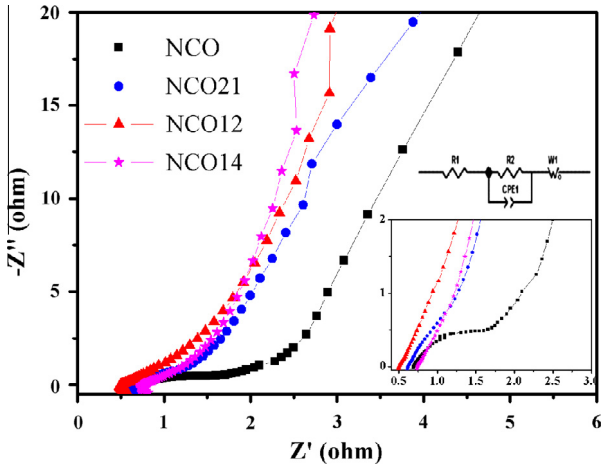

Fig. 7. Electrochemical impedance spectra (EIS) obtained from NCO, NCO21, NCO12, and NCO14 electrodes. The inset shows the enlarged EIS of the electrodes.

electro-active species [34]. All the samples show the similar slope of the straight line, meaning that the ion diffusions are in the same type. The intercept at the real part (Zre) is the total electric series resistance (ESR), which is a combination of the electrolyte resistance, contact resistance at interface, and the intrinsic resistance of the electrode [35,36]. In the inset images, the intercept with real axis of NCO12 is the smallest, illustrating that the higher electrical conductivity of NCO12. It is also due to the unique porous structure.

Based on the above electrochemical analysis, NCO12 shows superior capacitive and cycling performance even at considerably high charge and discharge currents. The reasons can be well understood if the following factors are considered. First, the porous structure owns a large SSA and suitable pore size, which can enlarge the contact area with the electrolyte and increase more active sites for redox reaction. Second, the porous structure exhibits a 3D network to provide electron more tunnels for electrons and ions transport. Third, $NiCo_2O_4$ composites possess higher electric conductivity.

4. Conclusions

We demonstrated an effective strategy for preparing the 3D porous structural $NiCo_2O_4$ composite and preventing the NCO from aggregation via a template method under facile conditions. SiO_2 sol was used as the template to create pores in the NCO composites and avoid the aggregation of NCO composites. The NCO grew on the surface of SiO_2 could transform their morphology from particles to nanosheets. Through controlling the ratio of SiO_2 and NCO, the porous structure could also be adjusted. A high specific capacitance of 1389 F g^{-1} can be achieved for NCO12 composite. The excellent electrochemical performance is a result of the synergetic effect. The binary system owns superiority over single oxides. The unique 3D structure provides more active sites and large contact area for redox reaction. Thus, the porous NCO12 composite shows higher specific capacitance, better cyclicity and stability, which is promising for large-capacity energy storage.

Acknowledgements

This work is supported by the National Basic Research Program of China (2012CB932303) and the National Natural Science Foundation of China (Grant No. 51072215 and 51172261) and the supporting from the committee of Shanghai Science and Technology (13XD1403900).

Appendix A. Supplementary material

Supplementary data associated with this article can be found, in the online version, at http://dx.doi.org/10.1016/j.jcis.2016.01.020.

References

[1] Z.Y. Lu, W. Zhu, X.D. Lei, G.R. Williams, D. O'Hare, Z. Chang, X.M. Sun, X. Duan, High pseudocapacitive cobalt carbonate hydroxide films derived from CoAl layered double hydroxides, Nanoscale 4 (12) (2012) 3640–3643.
[2] Sumanta Kumar Meher, P. Justin, G. Ranga Rao, Microwave-mediated synthesis for improved morphology and pseudocapacitance performance of nickel oxide, ACS Appl. Mater. Interfaces 3 (6) (2011) 2063–2073.
[3] C. Liu, F. Li, L.-P. Ma, H.-M. Cheng, Advanced materials for energy storage, Adv. Mater. 22 (8) (2010) E28–E62.
[4] L. Yuan, X.H. Lu, X. Xiao, T. Zhai, J. Dai, F. Zhang, B. Hu, X. Wang, L. Gong, J. Chen, C. Hu, Y. Tong, J. Zhou, Z.L. Wang, Flexible solid-state supercapacitors based on carbon nanoparticles/MnO_2 nanorods hybrid structure, ACS Nano 6 (1) (2012) 656–661.
[5] C.Y. Chen, C.Q. Chen, P.P. Huang, F.F. Duan, S.C. Zhao, P. Li, J.C. Fan, W.G. Song, Y. Qin, NiO/nanoporous graphene composites with excellent supercapacitive performance produced by atomic layer deposition, Nanotechnology 25 (50) (2014) 504001.
[6] Z. Lu, Q. Yang, W. Zhu, Z. Chang, J. Liu, X. Sun, D.G. Evans, X. Duan, Hierarchical Co_3O_4@Ni–Co–O supercapacitor electrodes with ultrahigh specific capacitance per area, Nano Res. 5 (5) (2012) 369–378.
[7] Y. Wang, H. Liu, X. Sun, I. Zhitomirsky, Manganese dioxide–carbon nanotube nanocomposites for electrodes of electrochemical supercapacitors, Scr. Mater. 61 (11) (2009) 1079–1082.
[8] M. Zhi, C. Xiang, J. Li, M. Li, N. Wu, Nanostructured carbon–metal oxide composite electrodes for supercapacitors: a review, Nanoscale 5 (1) (2013) 72–88.
[9] J.H. Zhong, A.L. Wang, G.R. Li, J.W. Wang, Y.N. Ou, Y.X. Tong, Co_3O_4/$Ni(OH)_2$ composite mesoporous nanosheet networks as a promising electrode for supercapacitor applications, J. Mater. Chem. 22 (12) (2012) 5656–5665.
[10] J. Chen, D.H. Bradhurst, S.X. Dou, H.K. Liu, Nickel hydroxide as an active material for the positive electrode in rechargeable alkaline batteries, J. Electrochem. Soc. 146 (10) (1999) 3606–3612.
[11] X. Ma, Y. Dai, L. Yu, B. Huang, Noble-metal-free plasmonic photocatalyst: hydrogen doped semiconductors, Sci. Rep. 4 (2014) 3986.
[12] X. Ma, Y. Dai, B. Huang, Origin of the increased photocatalytic performance of TiO_2 nanocrystal composed of pure core and heavily nitrogen-doped shell: a theoretical study, ACS Appl. Mater. Interfaces 6 (24) (2014) 22815–22822.
[13] C. Yuan, J. Li, L. Hou, X. Zhang, L. Shen, X.W.D. Lou, Ultrathin mesoporous $NiCo_2O_4$ nanosheets supported on Ni foam as advanced electrodes for supercapacitors, Adv. Funct. Mater. 22 (21) (2012) 4592–4597.
[14] F. Yang, J.Y. Yao, F.L. Liu, H.C. He, M. Zhou, P. Xiao, Y.H. Zhang, Ni–Co oxides nanowire arrays grown on ordered TiO_2 nanotubes with high performance in supercapacitors, J. Mater. Chem. A 1 (3) (2013) 594–601.
[15] H. Gao, G. Wang, M. Yang, X. Zhang, Z. Shi, C. Li, X. Zhang, X. Cui, One-step fabrication of 3D hierarchical Ni-incorporated β-$Co(OH)_2$ assembled by 2D center disk and 1D length-tunable brush, RSC Adv. 3 (8) (2013) 2604–2612.
[16] H. Gao, G. Wang, M. Yang, L. Tan, J. Yu, Novel tunable hierarchical Ni–Co hydroxide and oxide assembled from two-wheeled units, Nanotechnology 23 (1) (2012) 015607.
[17] J. Xiao, S. Yang, Sequential crystallization of sea urchin-like bimetallic (Ni, Co) carbonate hydroxide and its morphology conserved conversion to porous $NiCo_2O_4$ spinel for pseudocapacitors, RSC Adv. 1 (4) (2011) 588.
[18] T.Y. Wei, C.H. Chen, H.C. Chien, S.Y. Lu, C.C. Hu, A cost-effective supercapacitor material of ultrahigh specific capacitances: spinel nickel cobaltite aerogels from an epoxide-driven sol–gel process, Adv. Mater. 22 (3) (2010) 347–351.
[19] L. Qie, W.M. Chen, H.H. Xu, X.Q. Xiong, Y. Jiang, F. Zou, X.L. Hu, Y. Xin, Z.L. Zhang, Y.H. Huang, Synthesis of functionalized 3D hierarchical porous carbon for high-performance supercapacitors, Energy Environ. Sci. 6 (8) (2013) 2497–2504.
[20] L. Huang, D. Chen, Y. Ding, S. Feng, Z.L. Wang, M. Liu, Nickel–cobalt hydroxide nanosheets coated on $NiCo_2O_4$ nanowires grown on carbon fiber paper for high-performance pseudocapacitors, Nano Lett. 13 (7) (2013) 3135–3139.
[21] H. Wang, Z. Xu, A. Kohandehghan, Z. Li, K. Cui, X. Tan, T.J. Stephenson, C.K. King'ondu, C.M.B. Holt, B.C. Olsen, J.K. Tak, D. Harfield, A.O. Anyia, D. Mitlin, Interconnected carbon nanosheets derived from hemp for ultrafast supercapacitors with high energy, ACS Nano 7 (6) (2013) 5131–5141.
[22] L.L. Zhang, Z. Xiong, X.S. Zhao, A composite electrode consisting of nickel hydroxide, carbon nanotubes, and reduced graphene oxide with an ultrahigh electrocapacitance, J. Power Sour. 222 (2013) 326–332.
[23] X.H. Lu, D.Z. Zheng, T. Zhai, Z.Q. Liu, Y.Y. Huang, S.L. Xie, Y.X. Tong, Facile synthesis of large-area manganese oxide nanorod arrays as a high-performance electrochemical supercapacitor, Energy Environ. Sci. 4 (8) (2011) 2915–2921.
[24] L. Wang, X.H. Liu, X. Wang, X.J. Yang, L.D. Lu, Preparation and electrochemical properties of mesoporous Co_3O_4 crater-like microspheres as supercapacitor electrode materials, Curr. Appl. Phys. 10 (6) (2010) 1422–1426.
[25] H.S. Zhou, D.L. Li, M. Hibino, I. Honma, A self-ordered, crystalline-glass, mesoporous nanocomposite for use as a lithium-based storage device with both high power and high energy densities, Angew. Chem. – Int. Ed. 44 (5) (2005) 797–802.
[26] Zhong-Shuai Wu, W. Ren, Da-Wei Wang, Feng Li, Bilu Liu, Hui-Ming Cheng, High-energy MnO_2 nanowiregraphene and graphene asymmetric electrochemical capacitors, ACS Nano 4 (2010) 5835–5842.
[27] X. Sun, G.K. Wang, J.Y. Hwang, J. Lian, Porous nickel oxide nano-sheets for high performance pseudocapacitance materials, J. Mater. Chem. 21 (41) (2011) 16581–16588.
[28] X. Zhu, H. Dai, J. Hu, L. Ding, L. Jiang, Reduced graphene oxide–nickel oxide composite as high performance electrode materials for supercapacitors, J. Power Sour. 203 (2012) 243–249.
[29] X.H. Xia, J.P. Tu, Y.J. Mai, R. Chen, X.L. Wang, C.D. Gu, X.B. Zhao, Graphene sheet/porous NiO hybrid film for supercapacitor applications, Chem. – Eur. J. 17 (39) (2011) 10898–10905.
[30] S. Ghasemi, R. Ojani, S. Ausi, Bipotential deposition of nickel–cobalt hexacyanoferrate nanostructure on graphene coated stainless steel for supercapacitors, Int. J. Hydrogen Energy 39 (27) (2014) 14918–14926.
[31] B. Zhao, J. Song, P. Liu, W. Xu, T. Fang, Z. Jiao, H. Zhang, Y. Jiang, Monolayer graphene/NiO nanosheets with two-dimension structure for supercapacitors, J. Mater. Chem. 21 (46) (2011) 18792–18798.
[32] S.-E. Chun, S.-I. Pyun, G.-J. Lee, A study on mechanism of charging/discharging at amorphous manganese oxide electrode in 0.1 M Na_2SO_4 solution, Electrochim. Acta 51 (28) (2006) 6479–6486.
[33] Y.-Y. Horng, Y.-C. Lu, Y.-K. Hsu, C.-C. Chen, L.-C. Chen, K.-H. Chen, Flexible supercapacitor based on polyaniline nanowires/carbon cloth with both high

gravimetric and area-normalized capacitance, J. Power Sour. 195 (13) (2010) 4418–4422.
[34] L. Wang, Z.H. Dong, Z.G. Wang, F.X. Zhang, J. Jin, Layered α-$Co(OH)_2$ nanocones as electrode materials for pseudocapacitors: understanding the effect of interlayer space on electrochemical activity, Adv. Funct. Mater. 23 (21) (2013) 2758–2764.
[35] X. Sun, G. Wang, J. Hwang, J. Lian, Porous nickel oxide nano-sheets for high performance pseudocapacitance materials, J. Mater. Chem. 21 (41) (2011) 16581–16588.
[36] H. Chen, L. Hu, M. Chen, Y. Yan, L. Wu, Nickel–cobalt layered double hydroxide nanosheets for high-performance supercapacitor electrode materials, Adv. Funct. Mater. 24 (7) (2014) 934–942.